Supporting Information

Realizing a flexible and wavelength-tunable random laser inspired by cicada wing's replica

Chia-Jung Chou,[†] Ayano Abe,[‡] Jian-Fu Tang,[‖] Tzu-Chau Lin,[¶] Chi-Ching Kuo,[§] Ja-Hon Lin,[*,†] and Chihaya Adachi[*,‡]

[†]Department of Electro-Optical Engineering, National Taipei University of Technology, Taipei, Taiwan

[‡]Center for Organic Photonics and Electronics Research (OPERA), Kyushu University, Motooka, Nishi-ku, Fukuoka, Japan

[‖]Department of Electronic Engineering, Lunghwa University of Science and Technology, Taoyuan, Taiwan

[¶]Department of Chemistry, Photonic Materials Research Laboratory, NCU-Covestro Research Center, National Central University, Taoyuan, Taiwan

[§]Institute of Organic and Polymeric Materials, National Taipei University of Technology, Taipei, Taiwan

E-mail: jhlin@ntut.edu.tw ; adachi@cstf.kyushu-u.ac.jp

Molecule structure of LDS 722

LDS722 belongs to the hemicyanine series of dyes, which contains donor and acceptor units separated by intervening π bonds. The molecular structure of LDS 722 is shown in Fig. S1.

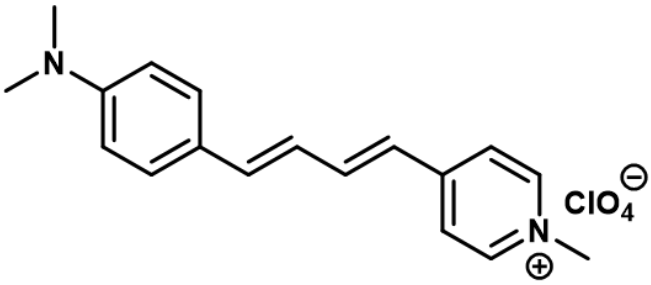

Figure S1. Molecule structure of LDS722.

SEM image of cicada`s wing and replica film

Figures S2(a)-(c) shows the SEM images of the cicada's wing, PDMS negative template, and SFRF. It is evident from the images that there is a quasi-periodic arrangement of nano-papillae on both the cicada's wing and the SFRF.

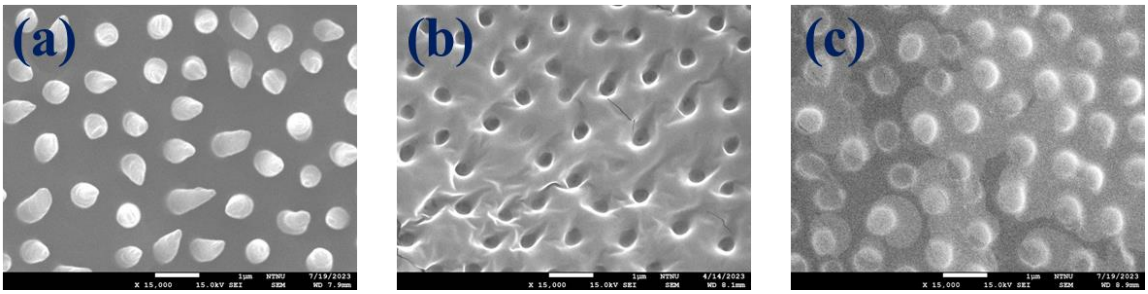

Figure S2. SEM images of (a) cicada's wing, (b) PDMS negative template and (c) SFRF from cicada's wing.

Water contact angle of cicada`s wing and film

Water contact angle measurements are crucial for evaluating the hydrophobicity of surface on materials or devices. Larger contact angles indicate stronger hydrophobic properties. Due to the surface chemistry and the surface nanopapillate structures, the original cicada wing shows hydrophobicity with the large water contact angle of around 120.4° as shown in Fig. S3 (a). In Fig. S3 (b), the contact angle of the complementary PDMS replica film is observed to be 113.3°, slightly lower than that of the original cicada wing. The SFRF possesses nanopapillate structures that mimic the topography of cicada wings, achieving a contact angle of 102.7° as shown in Fig. S3 (c). In contrast, the pure SFF is hydrophilic, displaying a low contact angle of approximately 52.4°, as shown in Fig. S3(d). Table S1 shows the water contact angles of replica films made from cicada's wings using various materials as reported in previous studies [1-4], including PDMS, Polyvinyl Chloride (PVC), Polystyrene (PS) and Polypropylene (PP). It shows that the great improvement of water contact angle from SFF to SFRF with a significant increase rate of up to 99.8%, confirming the successful replication of nanostructures from cicada`s wing.

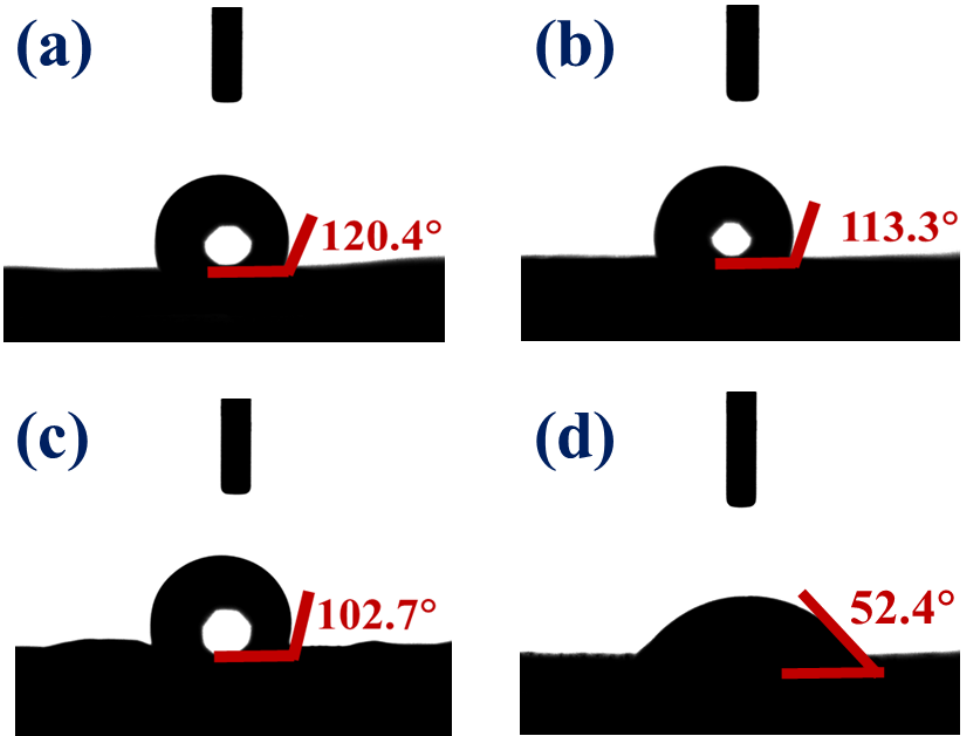

Figure S3. Water contact angle of (a) cicada's wing, (b) PDMS negative template, (c) SF RF from cicada's wing and (d) pure SFF.

Table S1. Comparison of water contact angles of replica films from cicada's wing fabrication using different materials.

Sample	Origin	Replica	Increase rate (%)	Source
SF	52.4°	102.7°	99.8%	Our work
PDMS	105°	143°	36.2%	[1]
PVC	86°	132°	53.4%	[2]
PS	83°	143°	72.3%	[3]
PP	85°	128°	50.6%	[4]

Speckle noise reduction from the replica film

In this work, we demonstrated speckle noise reduction image by means of the bio-inspired scattering device comprising nanopapillate, which was produced by the nanocasting from on cicada`s wing. Figure S4(a) illustrates the schematic setup for generating a speckle reduction image using a green continuous-wave laser (532 nm) as the light source through micro-vibrations on SFRF. The produced SFRF was affixed to a piezoelectric ceramic transducer (PZT) and positioned after the laser to serve as scattering device. The scattering beamlet from screen was captured by the charge-coupled device (CCD, THORLABS, DCC1240C, pixel size: 1280 x 1024). After applying voltage onto the PZT, the scatter was shaken to form a micro-vibration. Without insertion of scatter, an obviously granular patterns were revealed from the projected image in Fig. S4(b), which degrades image quality. Upon the insertion of the SFF and SFRF as a light scatter, the size of granular patterns was reduced, leading to an improved image discrimination as depicted in Figs. S3 (c) and (d). This change was accompanied by a reduction in contrast (C_T) from 0.212 to 0.119 and 0.073. As the applied voltage (V_{ap}) of the PZT increases from 1V to 5V, it leads to an increase in the vibration amplitude of the SFRF. Consequently, the size and number of granular patterns were significantly reduced as depicted in Figs. S4 with (e) V_{ap} =1V, (f) V_{ap} =2V, (g) V_{ap} =3V, (h) V_{ap} =4V, and (i) V_{ap} =5V. It results in a smoother image and a

further reduction in contrast, reaching approximately 0.052 as V_{ap} =5V.

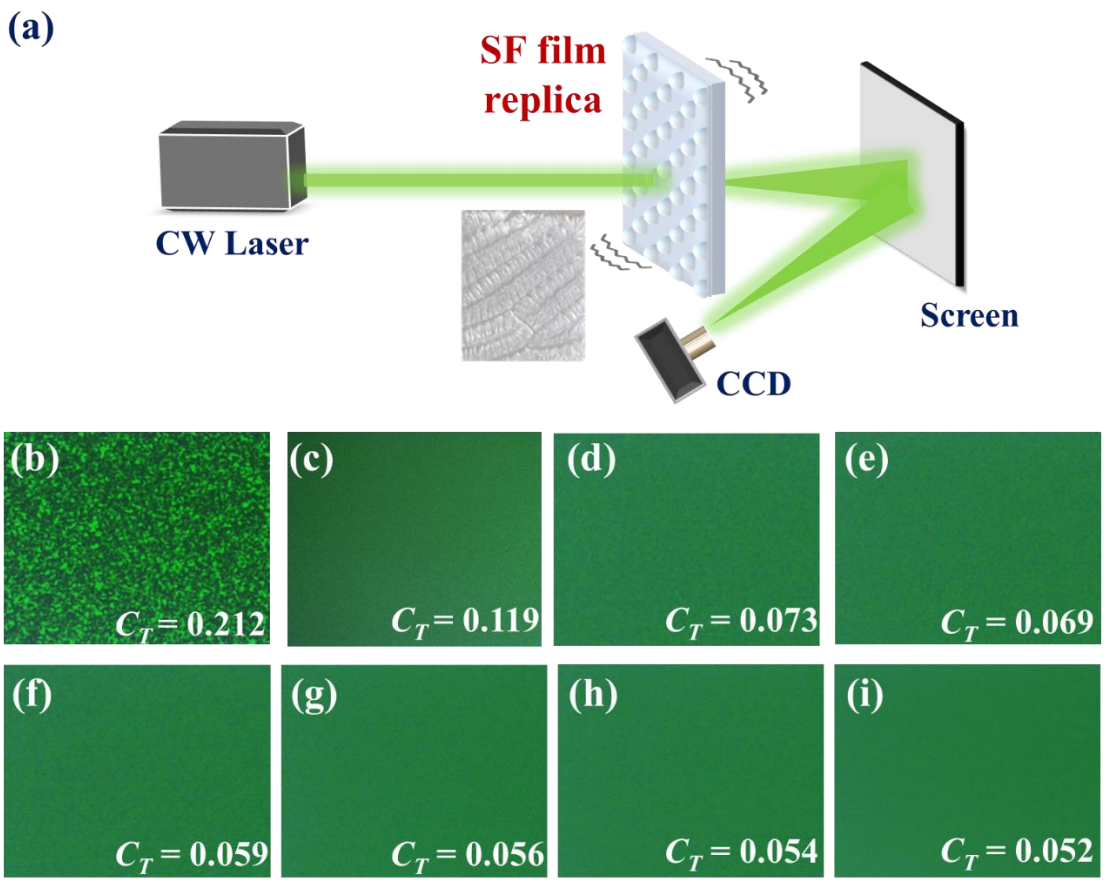

Figure S4(a) Illustration of the experimental setup for the measurement of speckle-noise pattern. The captured speckle pattern and the estimated contrast (b) without scatter, and (c) with insertion of SFR, with insertion of SRRF (d) without applied voltage (V_{ap} = 0V), and as the applied voltage increases to (e) V_{ap} = 1V, (f) V_{ap} = 2V, (g) V_{ap} = 3V, (h) V_{ap} = 4V, (i) V_{ap} = 5V.

Speckle image from the replica film

Figures S5 (a)-(c) also show the captured speckle image of the AF chart under illumination of CW laser (a) without SFRF, with SFRF (b) without applied voltage (V_{ap} = 0V), and (c) with 5V applied voltage to the PZT (V_{ap} = 5V) to cause the vibration of SFRF. The pattern on the test chart was captured by a CCD camera (DCC3240N, Thorlabs Inc.) through an objective lens (Obj, 5X).

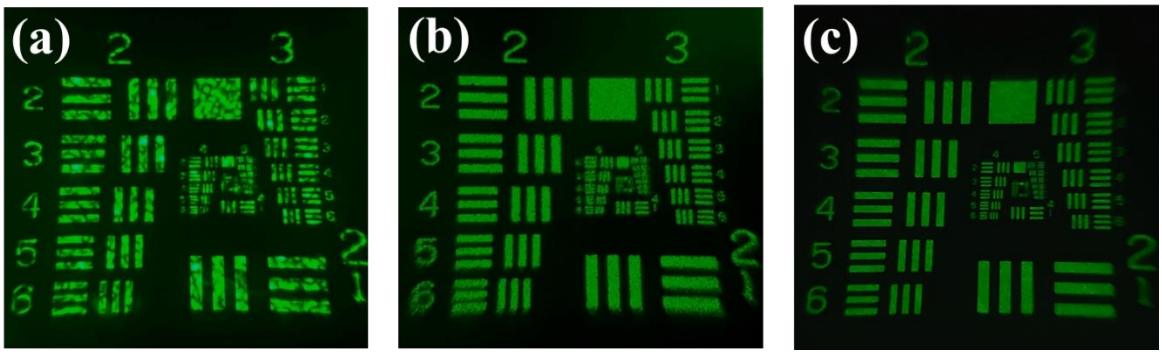

Figure S5 The captured speckle image from the AF chart under illumination of CW laser (a) without SFRF, (b) with SFRF without applied voltage (V_{ap} = 0V), and (c) with SFRF using a 5V applied voltage to the PZT (V_{ap} = 5V).

Refractive index of organic laser dye

The refractive index of an organic dye was obtained through measurement using ellipsometry (M-2000VI, J.A.Woollam Inc.). To conduct the measurement, organic dye LDS 722 was coated on a pure silica glass substrate. Figure S6 shows the refractive index of organic dye LDS 722 as a function of wavelength. The refractive index of material varies with wavelength according to the Cauchy's relation: $n\,(\lambda) = A + B/\lambda^2$, where A = 1.56 and B = 0.006 represent the empirical constants specific to the material. By applying this relationship, the refractive index at the wavelength of 715 nm was found to be approximately 1.79.

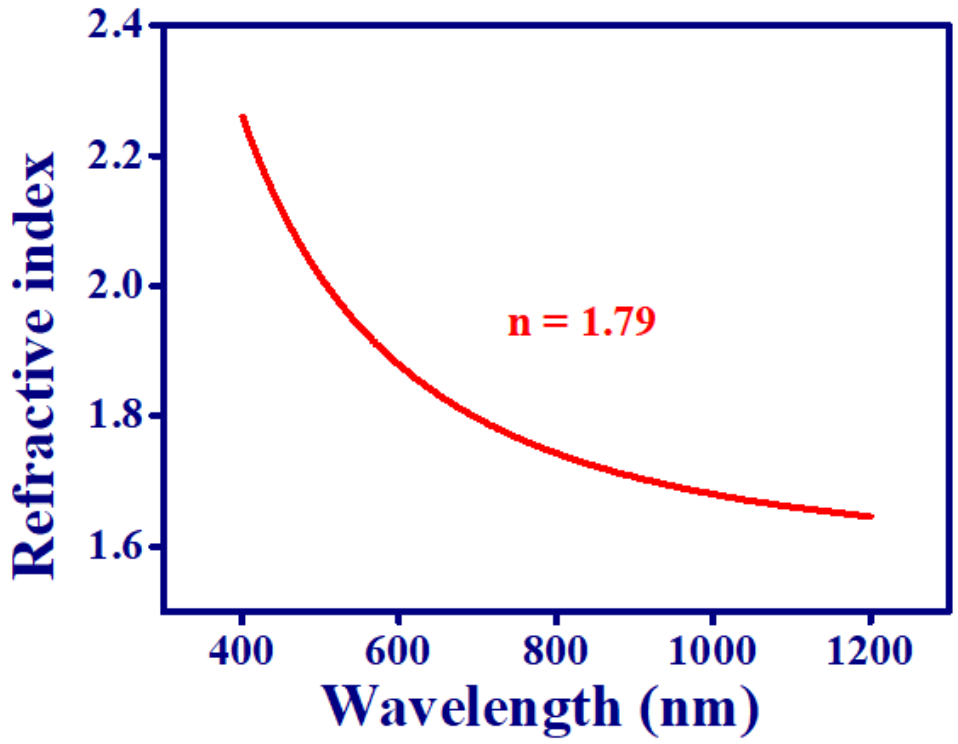

Figure S6 Refractive index of LDS722 as a function of wavelength.

Photostability of RLs from DS-SFF and DC-SFRF

The photostability of RL from SFRF and SFF is illustrated below. It is observed that the energy of SFRF decreases to half of its original value after 4.8×10^4 excitation shots in Fig. S7(b). In contrast, the energy decline of SFF in Fig. S7(a) is more rapid, reaching half of its initial energy after 2.7×10^4 pulse excitations. The enhanced stability of SFRF may be attributed to heightened light scattering from nanopapillate structures, effectively mitigating heat accumulation during higher excitation pump pulses and consequently reducing sample degradation.

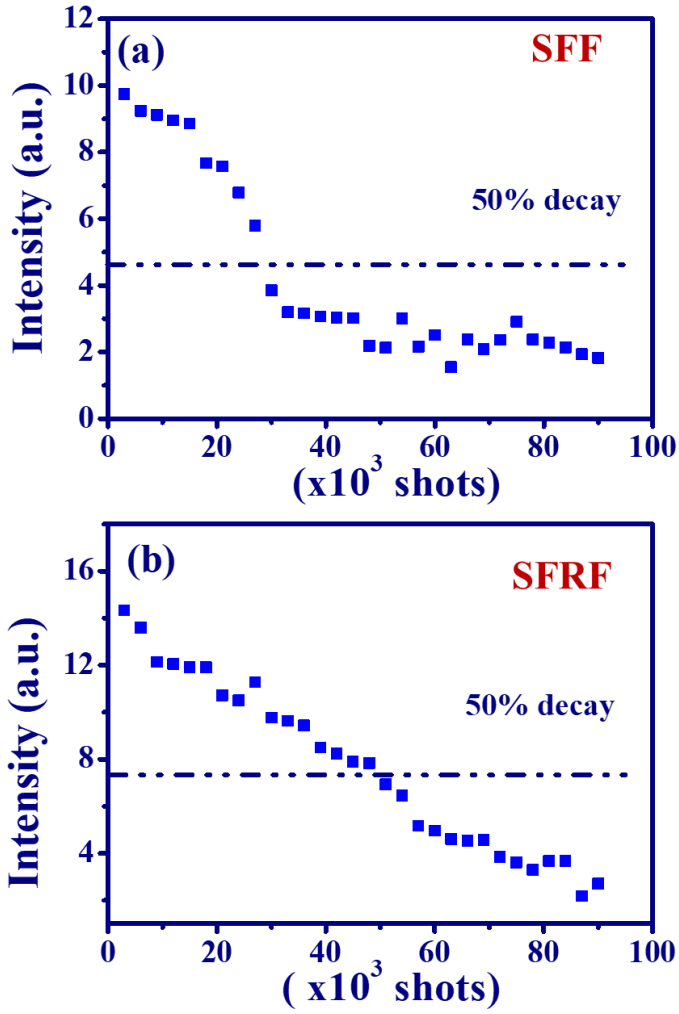

Fig. S7 Intensity variation of RL as function of the number of pump pulses excitation for (a) SFF, and (b)SFRF.

Variation of emission spectrum under the rotation of the linear polarizer

Figure S8 (a) depicts the experimental setup used to obtain the polarization characteristics of the RL generated from DC-SFF and DC-SFRF, in which a linear polarizer (LP) was placed in front of the fiber tip. We measured the emission spectrum component while rotating the LP. Figures S8(b) and (c) show the variation of emission spectrum component from DC-SFF and DC-SF RF as a function of the rotation angle (ϕ). Here the rotation angle (ϕ) is the included angle between linear polarizer and surface normal of optical table. The results clear show that the peak intensity reaches its maximum value when the LP at an angle of 0°, and gradually decreases as the LP is rotated to 90°.

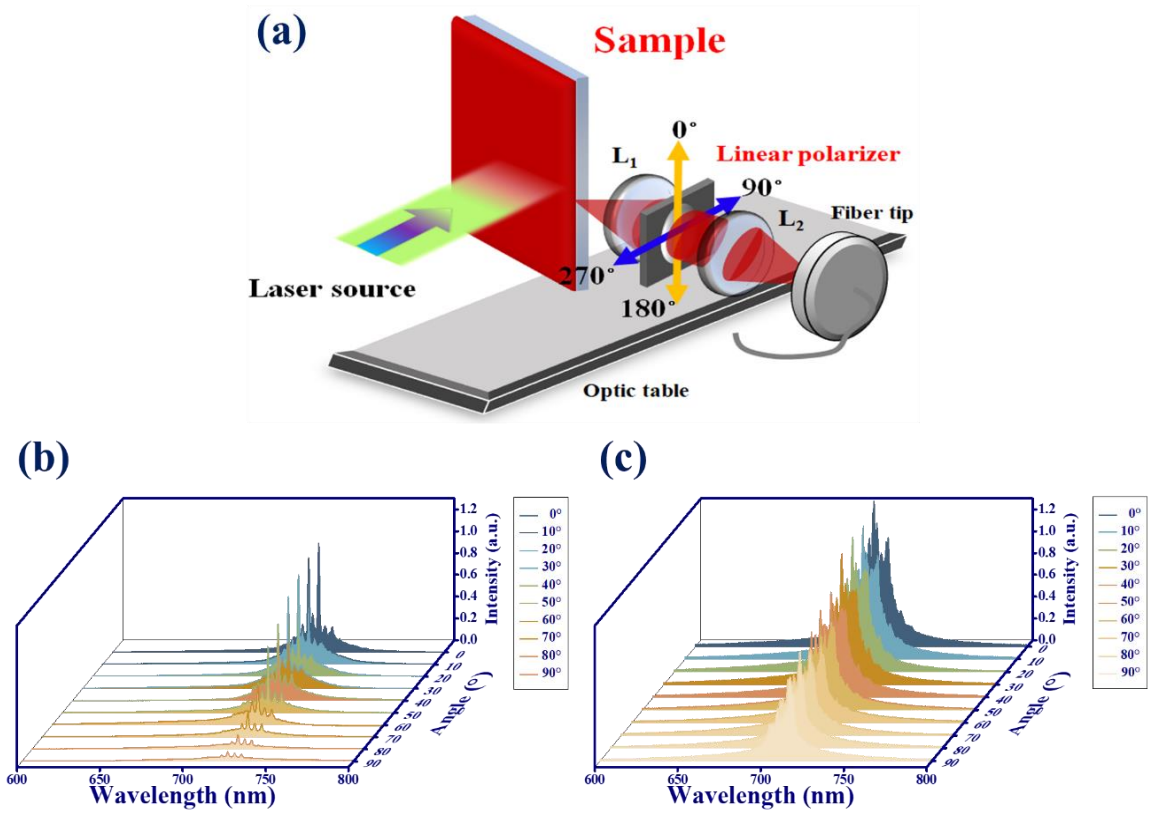

Figure S8 (a) Schematic setup to obtain the polarization of RL, and the progression of emission spectrum with respect to the rotation angle ϕ from RLs of (b) DC-SFF and (c) DC-SFRF.

Variation of emission spectrum under different emission angle

In contrast to the conventional lasers with high directionality, the output of RLs exhibits a broad emission angle. To confirm the emission angle of RL from the two samples, the experimental setup is depicted in Fig. 4(c). Here, θ is defined as the observation angle between the detector and the x-axis, which is parallel to the sample surface. Figures S9 (a) and (b) display the lasing emission spectra from the DC-SFF and DC-SFRF versus the observation angle (θ).

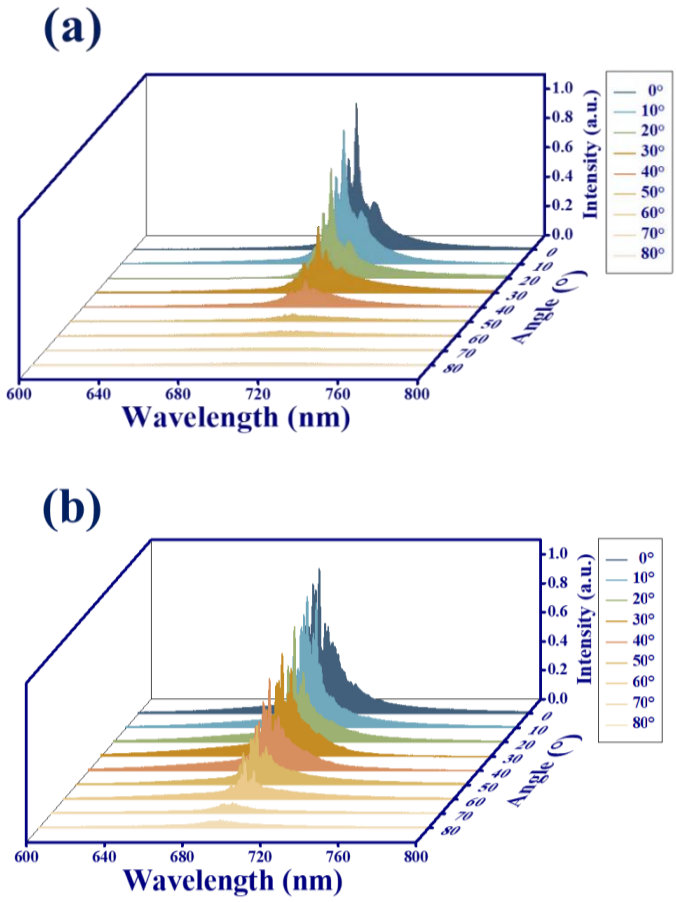

Figure S9 The progression of emission spectrum with respect to the emission angle from RLs of (a) DC-SFF and (b) DC-SFRF.

Flexible RL speckle image under different curvature

Figures S10(a)-(j) reveal the speckle images of bent DC-SFRF RL under various curvatures. Inset figure shows the grabbed intensity fluctuation (wheat line) in the center of speckle image. It is clear to see the fluctuation amplitude decrease as curvature increases. In addition, the estimated speckle contrast (C_T) of the DC-SFRF decreases from 0.040 to 0.031 as the curvatures (C_V) increase to 2.85 cm^{-1}.

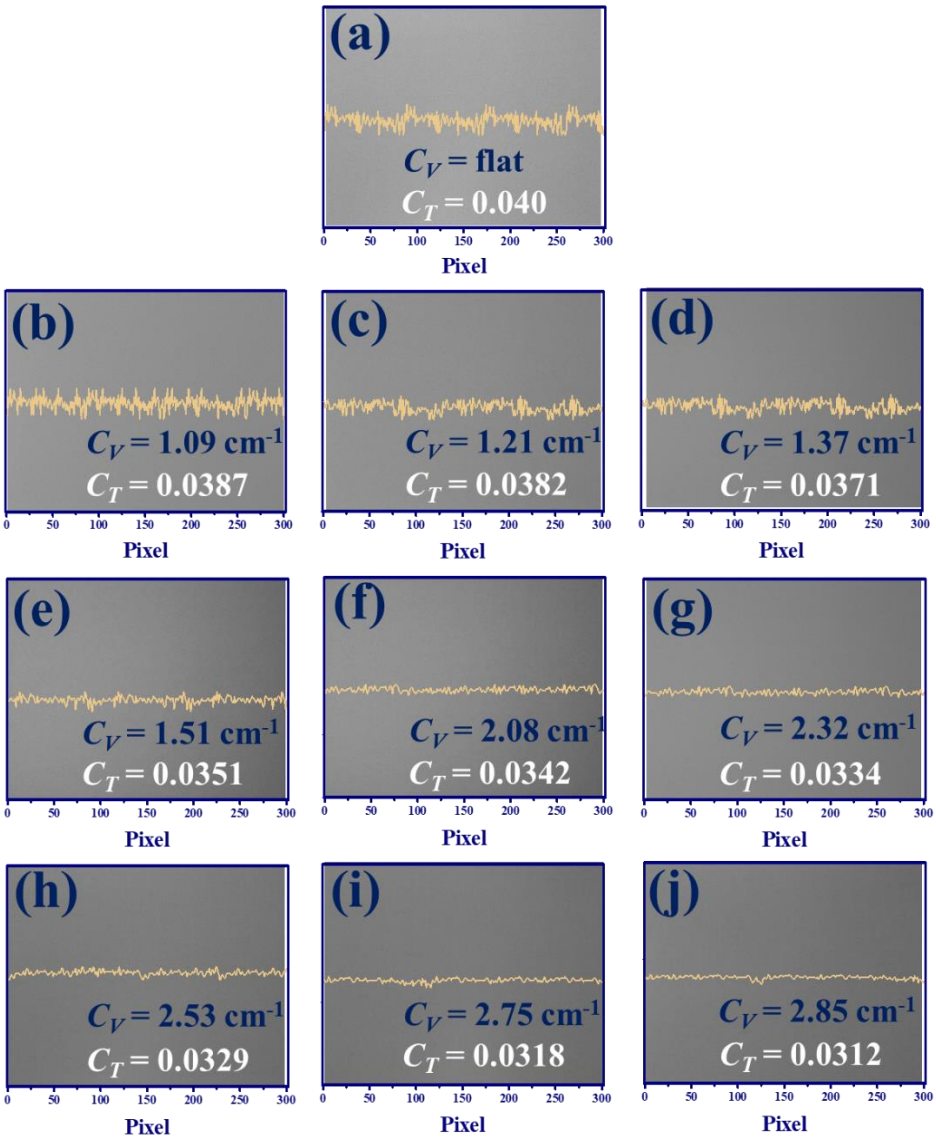

Figure S10 The captured speckle patterns, using the flexible RL as a light source, exhibit changes as the curvature (C_V) of DC-SFRF varies, with the curvatures shown at (a) infinity (without bending), (b) 1.09 cm^{-1}, (c) 1.21 cm^{-1}, (d) 1.37 cm^{-1}, (e) 1.51 cm^{-1}, (f) 2.08 cm^{-1}, (g) 2.32 cm^{-1}, (h) 2.53 cm^{-1}, (i) 2.75 cm^{-1} and (j) 2.85 cm^{-1}.

Reference

1. Watson, G.S., et al., *Putative functions and functional efficiency of ordered cuticular nanoarrays on insect wings.* Biophys J, 2008. **94**(8): p. 3352-60.
2. Hong, S.H., J. Hwang, and H. Lee, *Replication of cicada wing's nano-patterns by hot embossing and UV nanoimprinting.* Nanotechnology, 2009. **20**(38): p. 385303.
3. Xie, H., H.X. Huang, and Y.J. Peng, *Rapid fabrication of bio-inspired nanostructure with hydrophobicity and antireflectivity on polystyrene surface replicating from cicada wings.* Nanoscale, 2017. **9**(33): p. 11951-11958.
4. Xie, H., et al., *Tunable fabrication of biomimetic polypropylene nanopillars with robust superhydrophobicity and antireflectivity.* Nanotechnology, 2021. **32**(39).